A Deep Blue B,N-Doped Heptacene Emitter That Shows Both Thermally Activated Delayed Fluorescence and Delayed Fluorescence by Triplet−Triplet Annihilation

Subeesh Madayanad Suresh, Eimantas Duda, David Hall, Zhen Yao, Sergey Bagnich, Alexandra M. Z. Slawin, Heinz Bässler, David Beljonne, Manfred Buck,* Yoann Olivier,* Anna Köhler,* and Eli Zysman-Colman*

Read Online

ACCESS | Metrics & More | Article Recommendations | Supporting Information

ABSTRACT: An easy-to-access, near-UV-emitting linearly extended B,N-doped heptacene with high thermal stability is designed and synthesized in good yields. This compound exhibits thermally activated delayed fluorescence (TADF) at ambient temperature from a multiresonant (MR) state and represents a rare example of a non-triangulene-based MR-TADF emitter. At lower temperatures triplet−triplet annihilation dominates. The compound simultaneously possesses narrow, deep-blue emission with CIE coordinates of (0.17, 0.01). While delayed fluorescence results mainly from triplet−triplet annihilation at lower temperatures in THF solution, where aggregates form upon cooling, the TADF mechanism takes over around room temperature in solution when the aggregates dissolve or when the compound is well dispersed in a solid matrix. The potential of our molecular design to trigger TADF in larger acenes is demonstrated through the accurate prediction of ΔE_{ST} using correlated wave-function-based calculations. On the basis of these calculations, we predicted dramatically different optoelectronic behavior in terms of both ΔE_{ST} and the optical energy gap of two constitutional isomers where only the boron and nitrogen positions change. A comprehensive structural, optoelectronic, and theoretical investigation is presented. In addition, the ability of the achiral molecule to assemble on a Au(111) surface to a highly ordered layer composed of enantiomorphic domains of racemic entities is demonstrated by scanning tunneling microscopy.
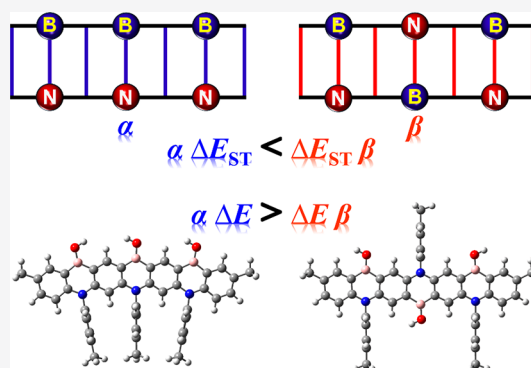
INTRODUCTION

The high charge carrier mobility of graphene[1,2] is an extremely appealing property that can be exploited in electrode design[3] for optoelectronic devices. To extend the applicability of graphene and its derivatives, the structure of the materials must be modified to modulate their band gaps. Reducing the dimensionality of graphene in the form of graphene quantum dots and graphene nanoribbons is one way to induce a defined band gap that overlaps with the visible spectrum in these materials.[4] Another strategy to modulate the optoelectronic properties of nanographenes, which are graphenoid fragments, involves heteroatom doping. In particular, boron-, nitrogen-, sulfur-, and phosphorus-doped organic nanographene materials have been identified as possessing useful properties in energy-related research such as supercapacitors,[5−8] lithium ion batteries,[9−12] fuel cells,[13−16] solar cells,[17−19] and sensors.[20−23] Recent advances in synthetic methodology in the form of surface-assisted coupling[24−27] or amplified growth[28−30] have permitted access to heteroatom-doped nanographene materials. The smallest heteroatom-doped nanographene compounds are frequently readily synthesized in good yields by using intra-

molecular Friedel−Crafts-type reaction. However, this synthetic approach demands the availability of electron-rich precursor molecules containing functional groups such as hydroxyl,[31,32] amino,[33−37] imino,[38,39] halogeno,[40−42] or trimethylsilyl groups,[43,44] which necessitates often a multistep synthesis of these precursors.

In 2015, Hatakeyama et al.[45] introduced a one-step borylation method to generate polycyclic aromatic hydrocarbons (PAHs) with a 1,4-oxoborine substructure through ortho-lithiation of 1,4-diaryloxybenzenes and subsequent transmetalation to boron, followed by electrophilic borylation of the arene. Later, the same group demonstrated the versatility and the impact of the one-step borylation through the synthesis of boron- and nitrogen-containing PAHs, which they showed to be high-
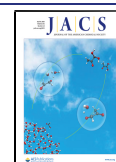
Previous work
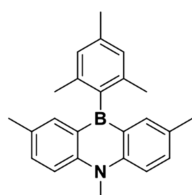
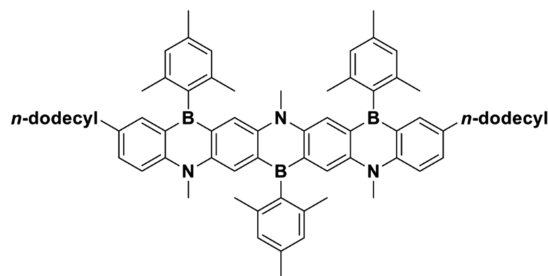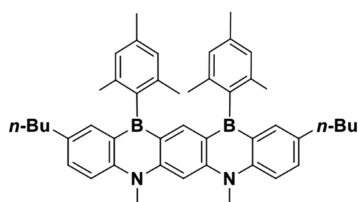**9**, λ_{PL} = 421 nm,
Φ_{PL} = 48%, cyclohexane
Fluorescent
Org. Lett., **2006**, *8*, 2241-2244

8, λ_{PL} = 625 nm,
Φ_{PL} = 55%, cyclohexane
Fluorescent
Org. Lett., **2006**, *8*, 2241-2244

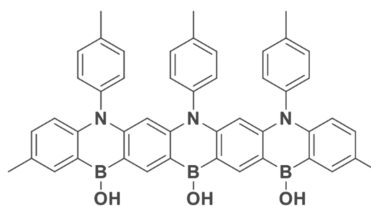**4**, λ_{PL} = 428 nm,
Φ_{PL} = 21%, cyclohexane
Fluorescent
Org. Lett., **2006**, *8*, 2241-2244
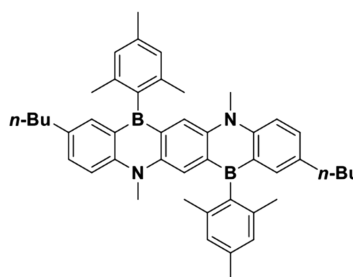
3, λ_{PL} = 534 nm,
Φ_{PL} = 69%, cyclohexane
Fluorescent
Org. Lett., **2006**, *8*, 2241-2244

Present work

α-**3BNOH**, λ_{PL} = 390 nm (300 K)
Φ_{PL} = 38% (Air), 50% (N_2), THF
TADF

Figure 1. Chemical structures of previously reported B,N-doped acenes and the structure of our molecule.

performance blue-emitting thermally activated delayed fluorescence (TADF) materials for organic light-emitting diodes (OLEDs). The synthetic protocols were further simplified, and a series of B,N-doped nanographenes could be obtained in a two-step synthesis consisting of a key multiborylation of a triarylamine intermediate. By adjusting the boron source, Brønsted base, and reaction temperature, selectively doublely and triply borylated products could be obtained.[45−50]

Among the striking advantages of these molecules is their narrow emission spectra (FWHM = 14−40 nm) compared to the conventional donor−acceptor TADF molecules (FWHM = 70−100 nm) because of their low reorganization energy. The origin of the TADF in these compounds originates from the combination of short-range charge transfer and delocalized hole and electron wave functions that effectively reduces the exchange and the singlet−triplet energy gap while maintaining a large radiative decay rate.[51] Since 2016, a number of improved-performance B,N-doped analogues all showing multi-resonant

TADF (MR-TADF) have been developed as emitters for OLEDs.

Incorporating main group elements into the framework of larger acenes was previously known as a very effective strategy to tune the property of the parent π-conjugated systems,[52] which are otherwise inaccessible in non-heteroatom-doped acenes. In particular, the integration of tricoordinate boron atoms within the PAH can result in the emergence of new optoelectronic properties. In 2006, Kawashima et al. reported a series of ladder-type fused azaborines by extending the number of boron and nitrogen atoms in the aromatic acenes.[53] In each of the examples shown in Figure 1, the boron and nitrogen atoms are disposed *para* with respect to each other—a regiochemistry that is necessary but not sufficient to turn on TADF in multiresonance emitters. As the conjugation length of the B,N-doped acenes is extended in the series where the relative positions of the boron and nitrogen atoms alternate, there is a pronounced observed red-shift of the photoluminescence (PL) spectrum from **9** to **3** to **8**. Surprisingly, when there is a regioregular extension of the

Scheme 1. Synthesis of α-3BNOH^{a}
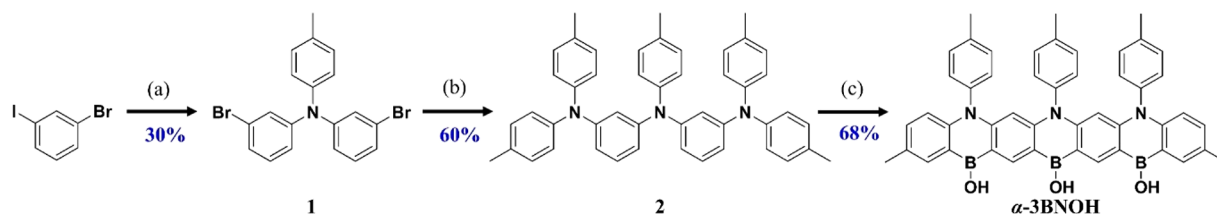
^{a}Reagents and conditions: (a) *p*-toluidine, Cu, CuI, K$_2$CO$_3$, reflux 5 days; (b) di-*p*-tolylamine, Pd(OAc)$_2$, [(*t*-Bu)$_3$PH]BF$_4$, NaO*t*-Bu, toluene, 110 °C, 24 h; (c) BBr$_3$, 1,2,4-trichlorobenzene, 200 °C, 12 h.
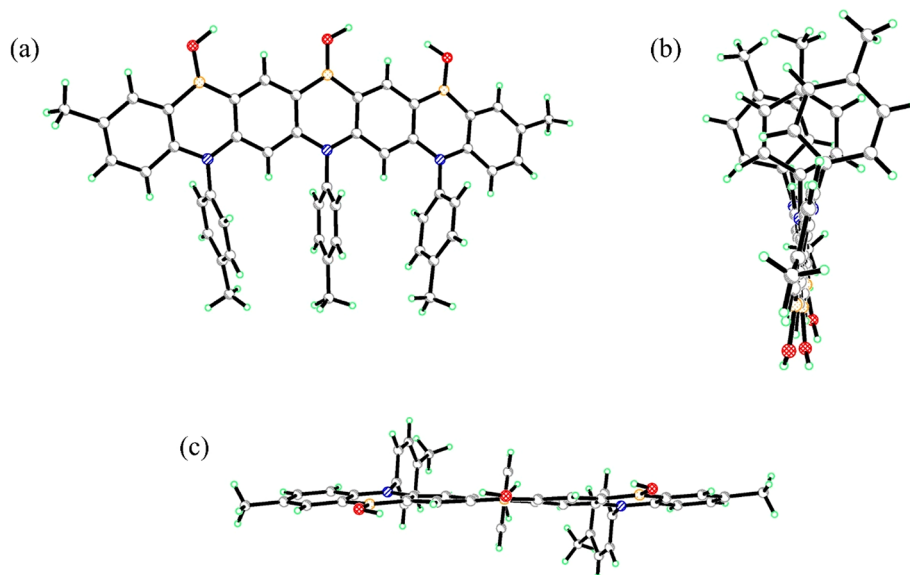

Figure 2. ORTEP diagram of (a) α-3BNOH obtained by single crystal X-ray analysis (b) and (c) side views. Thermal ellipsoids are displayed at 50% probability level.

B,N-doping, as in **4**, extended conjugation across the acene is suppressed, which leads to a very small red-shift of the PL spectrum upon extension of the acene (compare **3** vs **4**); these compounds were identified as fluorescent materials, and a detailed photophysical study of these B.N-doped acenes was not provided.

RESULTS AND DISCUSSION

In the context of our previous theoretical study that predicted that higher-order B,N-doped acenes should show promisingly small ΔE_{ST} and high oscillator strength, and mindful of the limited prior art summarized above, we targeted a linearly extended B−N-doped heptacene. Compound α-3BNOH was obtained from a 3-fold electrophilic borylation[49] of triamine **2** in good yield (Scheme 1), which itself was synthesized efficiently in two steps by a sequence of Ullman[54] and Buchwald−Hartwig[55] cross-coupling reactions. The OH functionalities are introduced during the isolation of α-3BNOH due to hydrolysis of the B−Br bonds. Extracting the crude reaction mixture in EtOAc followed by aqueous wash afforded crude α-3BNOH, which was then redissolved in MeCN and placed in an ultrasonic bath for 15 min. The formed off-white precipitate was then filtered and washed with acetonitrile, DCM, and hexane and dried to afford pure α-3BNOH. The identity and purity of α-3BNOH were established from a combination of ^{1}H and ^{13}C NMR spectroscopy, high-resolution mass spectrometry, elemental analysis, and single crystal X-ray diffraction analysis. High

thermal stability was noted for α-3BNOH based on thermogravimetric analysis (TGA). The decomposition temperature (T_d), defined as the 5% weight loss of the material, was calculated to be 554 °C (Figure S10).

Single crystal analysis was performed to identify the structural orientation of α-3BNOH (Figure 2) in the solid state. The three tolyl rings attached to the nitrogen are aligned nearly orthogonally (torsion angles: 86°−95°) to the heptacene core, which is likely to reduce the impact of possible $\pi-\pi$ interactions in the unit cell. The hydroxyl groups on the boron participate in hydrogen bonding with the THF solvent molecules in the crystal. There are no other intermolecular short contacts of note. In line with previous reports,[45,49] B−C (1.543−1.555 Å) bond lengths are longer than both C−C (1.388−1.421 Å) or C−N (1.392−1.444 Å) bonds present in the molecule. The heptacene core is nearly planar but bends because of the asymmetry in C−B−C and C−N−C bond angles due to the π-stacking interactions between the pendant phenyl rings.

We then applied spin-component scaling second-order approximate coupled-cluster (SCS-CC2) to model α-3BNOH as well as its alternative B,N-doped heptacene analogue, β-3BNOH (Figure 3). The difference density plots of both the S$_1$ and T$_1$ states are reminiscent of other MR-TADF emitters where there is an alternating pattern of increasing (in yellow) and decreasing (in green) density on adjacent atoms. A smaller ΔE_{ST} of 0.29 eV was calculated for α-3BNOH compared to that of β-3BNOH (ΔE_{ST} = 0.37 eV). Though somewhat higher than ideal
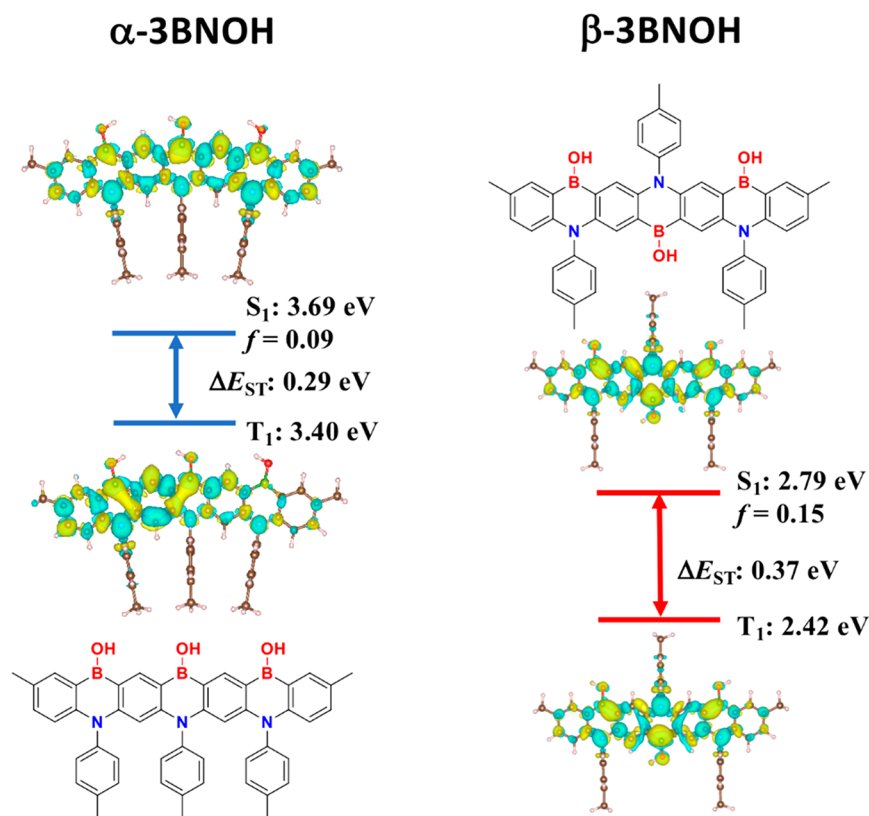
Figure 3. Different density plots for lowest singlet and triplet excited states for 3BNOH (linear, α-, and alternating, β-isomers) calculated in the gas phase by using SCS-CC2. Blue color represents an area of decreased electron density, and yellow represents an increased electron density between the ground and excited states.
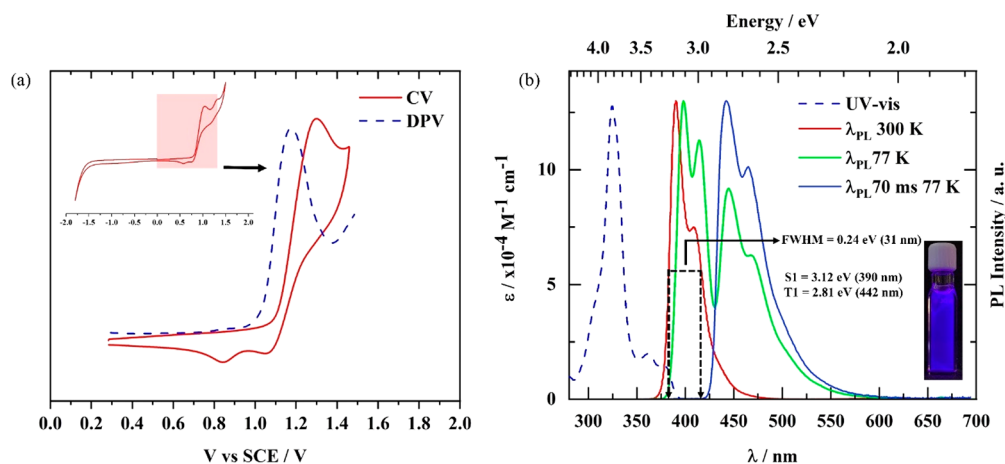

Figure 4. Solution-state optoelectronic measurements of α-3BNOH. (a) Cyclic and differential pulse voltammograms measured in degassed THF with 0.1 M $[nBu_4N]PF_6$ as the supporting electrolyte and Fc/Fc^+ as the internal reference (0.28 V vs SCE).[56] Scan rate = 100 mV s^{-1}. (b) Absorption, steady-state at 300 K, and emission at 77 K (steady-state and with 70 ms delay) measured in THF and steady-state emission at 300 K measured in PMMA (1 wt % emitter) spin-cast film. λ_{exc} = 325 nm. Inset shows PL of α-3BNOH in THF at 300 K.

for TADF emitters, we nevertheless expected that reverse intersystem crossing (RISC) would be thermally activated in α-3BNOH with potentially the assistance of higher-lying excited triplet states to the upconversion process (see Figure S12 for an energy diagram including higher-lying singlet and triplet excited states). A slightly larger oscillator strength, f, is predicted for β-3BNOH (0.15) compared to α-3BNOH (0.09). Most striking is the large change in the predicted energies of the excited states, with vertical excitation from S_0 to S_1 at 3.69 and 2.79 eV for α-3BNOH and β-3BNOH, respectively, corresponding to a

difference of 0.9 eV. This prediction is consistent with the observed red-shifting of the emission in the previously reported B/N-doped heptacenes (*vide supra*). The HOMO and LUMO electronic distribution is provided in the Supporting Information (Figure S11).

Having completed an *in silico* study of α-3BNOH with the alternating hypothetical analogue β-3BNOH, we now turn our attention to the optoelectronic properties of the title compound. The electrochemical behavior of α-3BNOH was measured by cyclic voltammetry (CV) and differential pulse voltammetry
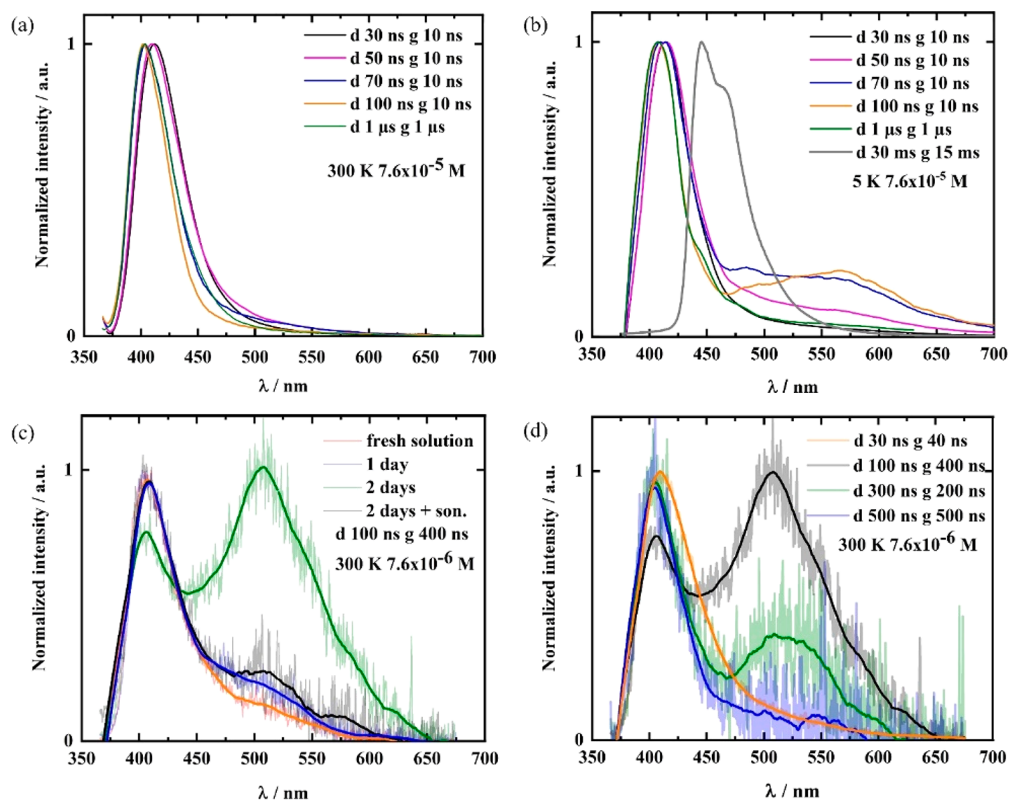
Figure 5. Emission spectra of α-3BNOH in THF at 7.6×10^{-5} M as indicated (a) at 300 K and (b) at 5 K for different delay times, d, and gate width, g (smoothed data). (c) At different times after preparation and after sonication (son), taken with a delay of 100 ns and a gate of 400 ns. (d) At 300 K for different delay times, d, and gate width, g, taken in a solution 2 days after preparation. The solid lines are smoothed curves through the lighter shaded data. For all data, λ_{exc} = 355 nm.

(DPV) in deaerated THF with 0.1 M tetra-*n*-butylammonium hexafluorophosphate as the supporting electrolyte (Figure 4a). The oxidation potential, E^{ox}, determined from the peak value of the first oxidation wave of the DPV curve is 1.17 V vs SCE, corresponding to a HOMO energy level of −5.97 eV (E_{HOMO} = −(E^{ox}_{onset} + 4.8) eV).[56,57] The oxidation is irreversible, and no reduction wave was found within the electrochemical window of the solvent. Therefore, the LUMO energy level of −2.81 eV was inferred by subtracting the optical energy gap, E_g, estimated from the onset of the absorption spectrum (E_g = 3.16 eV).

Figure 4b shows the photophysical properties of α-3BNOH in dilute THF solutions (10^{-5} M). The UV−vis absorption spectrum shows a strong absorption band at 3.84 eV (323 nm), assigned to a $\pi-\pi^*$ transition. The lowest-energy absorption band is found to be at 3.27 eV (379 nm) and is seen to arise from the combined contributions of the quasi-degenerate S_1 and S_2 excited states. Overall, this band appears to be significantly weaker compared to the low-energy absorption bands reported by Kawashima et al.[53] for compounds **3**, **4**, **8**, and **9** (Figure 1) where the most intense band was the lowest energy band. Quantitative agreement in the respective intensities and relative energy differences of the absorption bands is achieved between experiment and theory (see Figure S12). According to our SCS-CC2 calculations, S_1 to S_3 excited states are expected to contribute to the lowest-energy absorption bands due to their very close energies and oscillator strengths (S_1, S_2, and S_3 oscillator strengths are 0.09, 0.02, and 0.11, respectively) while the highest-energy absorption band is assigned to S_4 (oscillator strength of 0.65). The larger oscillator strength calculated for S_4 than for S_1 is explained by the larger overlap between the

HOMO−2 and LUMO+1 orbitals (see Figure S12 for the orbitals plots), which are involved in the dominant one-electron transition (54%) associated with S_4, resulting in a larger transition dipole moment in S_4 than in S_1. Similar to the emission profile reported for compound **8** (Figure 1), α-3BNOH shows structured emission. Both compounds are ladder-type heptacene-based molecules containing *para*-disposed boron and nitrogen atoms. Aside from the pattern of the boron and nitrogen atoms, structural differences include the substituents found at both nitrogen and boron; for compound **8**, mesityl groups are attached to boron and methyl groups are attached to nitrogen, while on α-3BNOH hydroxyl are substituted on boron and tolyl rings are connected to nitrogen. The photoluminescence spectrum at RT shows a structured profile with a sharp, near-UV emission band peaking at 3.18 eV (390 nm) and a shoulder at 3.03 eV (409 nm). Noteworthy is the very small full width at half-maximum (FWHM) of 0.24 eV (31 nm), which we attribute to the rigid nature of the compound that does not allow for torsional motions.[58−62] Because of the small Stokes shift of this emission and its short lifetime (see Figure 4b), we can assign this blue emission peaking at 3.18 eV (390 nm) at RT to fluorescence. By contrast, heptacene and its substituted derivatives absorb and emit in the red.[63−66] The second emission band, peaking at 2.81 eV (442 nm) with a shoulder at (465 nm) for 77 K, has a long lifetime of 310 ms (Figure 4b), as evident from its monoexponential decay curve (Supporting Information). Because of its well-resolved vibrational structure, the large shift from the fluorescence, and the long lifetime, it can be assigned to a triplet state. When measuring under steady-state conditions at 77 K, we observe
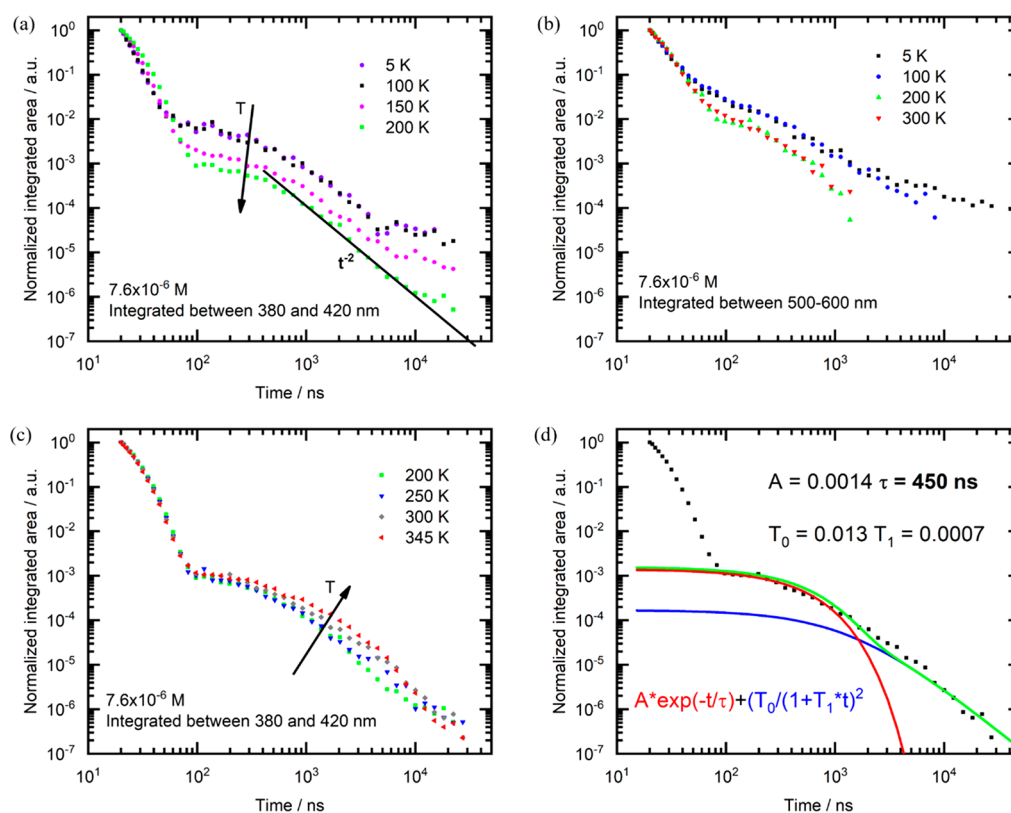
Figure 6. Photoluminescence transients taken in 7.6×10^{-6} M solution, excited at 355 nm; (a) integrated between 380 and 420 nm and taken upon heating from 5 to 200 K, with the green line indicating a slope of −2; (b) integrated between 500 and 600 nm and taken upon heating from 5 to 200 K; (c) integrated between 380 and 420 nm and taken upon heating from 200 to 345 K; (d) integrated between 380 and 420 nm at 300 K. The red curve represents a monoexponential, $A \exp(-t/\tau)$, while the blue curve represents a $[T_0/(1 + T_1 t)]^2$ fit, which is characteristic for the decay of a DF caused by TTA. The green line is the sum of red and blue lines. The fitting parameters are shown in the figure.

both the fluorescence and the phosphorescence components. The ΔE_{ST}, determined from the 0−0 peaks of the two bands at 77 K, is measured to be 0.31 eV, consistent with our SCS-CC2 calculations. The absolute photoluminescence quantum yield, Φ_{PL}, in 7.6×10^{-5} M THF at RT is 50%, which reduces to 38% upon exposure to air (Figure S13).

To obtain a deeper insight, we performed further photoluminescence measurements as a function of temperature, concentration, delay time after pulsed excitation, and gate width. Figure 5 shows the relevant spectra. For a 7.6×10^{-5} M solution at room temperature (Figure 5a), we observe essentially the same fluorescence spectrum for all delay times for short gate times of 10 ns, albeit there is some small hypsochromic shifting of the emission with increasing delay times. We point out that the resolution of the detector used for the time-resolved measurements of Figure 5 is lower than that of the spectrometer used for Figure 4, in particular in the blue spectral range. After a longer delay time of 1 μs and gate width of 1 μs, we still observe the same deep blue emission, which clearly indicates an origin that involves intermediate long-lived triplet states.

To observe phosphorescence, it is necessary to cool the solution, e.g., by forming a glass at 5 K (Figure 5b). By use of a long delay time of 30 ms and gate width of 15 ms, the structured phosphorescence spectrum is clearly visible. The fluorescence band shows the same small hypsochromic shift with increasing delay times as already observed at room temperature. In addition, a broad, unstructured band emerges in the green-to-red spectral range at short times that has fully disappeared by the microseconds time scale. The broadness and lack of feature

along with the red-shift compared to the fluorescence band near 400 nm and the intermediate lifetime of <1 μs is suggestive of an origin from a physical dimer or aggregate that may have formed when cooling; the driving force for aggregate formation at high dilution may be due in part to intermolecular hydrogen bonding as was observed by STM on gold surfaces (*vide infra*). To address this, we measured the PL in a freshly prepared, more dilute solution of 7.6×10^{-6} M, using a delay of 100 ns and a 400 ns gate width (Figure 5c). Around 500 nm, there is only a weak signal that can hardly be distinguished from the fluorescence tail (red curve). When repeating the measurement after 1 day (blue curve) and after 2 days (green curve), a band centered at 500 nm emerges. After sonication of the solution for a few minutes, this signal disappeared (black curve). On the basis of this observation, we associate the broad emission centered at 500 nm to interactions between adjacent chromophores, such as those prevailing in excimers, physical dimers, or aggregates.[62] As molecular motion or reorientation is severely restricted at 5 K, the most likely origin of the emission is rather weakly bound H-type aggregates. Figure 5d displays the PL spectra taken during several time intervals that evidence that the broad emission at 500 nm decays within 1 μs. It is remarkable that for these concentrations no such broad emission at 500 nm can be observed beyond 1 μs (also in the glass of Figure 5b), even though phosphorescence prevails on a milliseconds time scale. The lack of this broad emission and the rise of phosphorescence on a milliseconds time scale imply that aggregated molecules do not act as trap sites for triplet states. We could observe long-lived emission from aggregates, i.e., aggregate phosphorescence, only
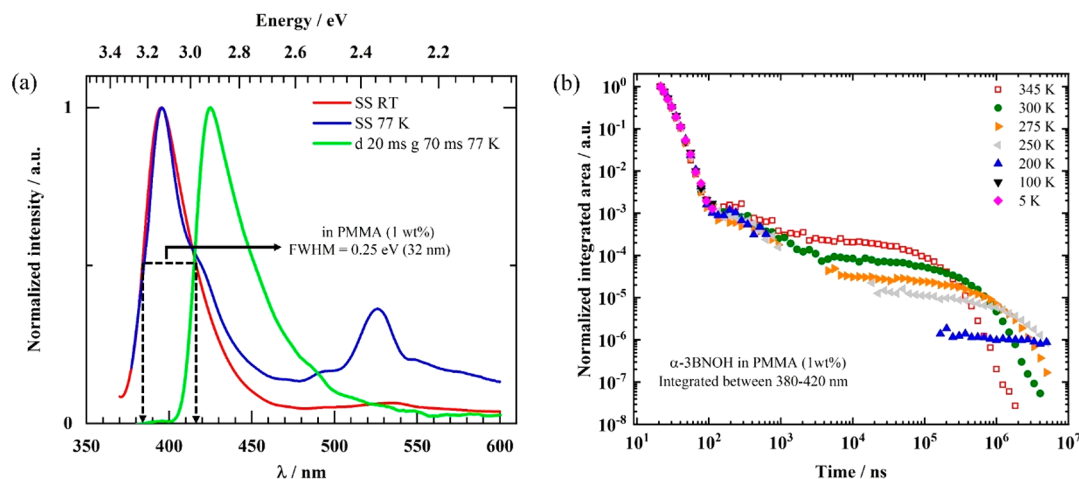
Figure 7. α-3BNOH dispersed at 1 wt %\ into PMMA. (a) Spectra taken under steady-state conditions at room temperature (red line, SS RT) and at 77 K (blue line, SS 77 K) and taken with a delay of 20 ms and a gate width of 70 ms at 77 K (green line). (b) Decay of the luminescence signal, spectrally integrated from 380 to 420 nm, taken at different temperatures as indicated.

when using more concentrated solutions or in thin films. This is detailed in the Supporting Information (Figure S14a,b). In passing, we mention that the singlet−triplet splitting in the aggregate is very small, on the order of about 70 meV.

Figure 6 addresses the luminescence transients. In the blue spectral window from 380 to 420 nm, the PL taken from a dilute 7.6×10^{-5} M solution shows a decay from prompt fluorescence followed by a delayed fluorescence component from about 50 ns onward (see Figure 6a). This DF decay has a very similar intensity at 5 and 100 K, yet it reduces relative to the prompt fluorescence upon heating to 150 and 200 K (see Figure 6b). We note that the glass transition temperature T_g of THF is about 120 K. The transient in the green-red spectral windows, 500−600 nm, shows a similar evolution insofar that the 5 and 100 K decays coincide, yet the relative intensity reduces upon heating to 200 and 300 K. The signal between 500 and 600 nm is due to aggregates, and we attribute the reduction of this signal upon heating to the dissociation of the aggregates with temperature. Recalling that for THF T_g is about 120 K, it is clear that this process only sets in from about 150 K onward. From the observation that the signal between 380 and 420 nm reduces in parallel to the signal between 500 and 600 nm upon heating, we conclude that the existence of aggregates is a prerequisite for the delayed blue emission up to and including 300 K.

The most likely origin is that the blue delayed fluorescence results from triplet−triplet annihilation (TTA) that can occur in the aggregated material, which forms despite the high dilution. We recall that at these concentrations the emissive aggregates do not provide a significant number of traps for the (monomer) triplet states. We have measured the dependence of the steady-state emission, i.e., the blue signal, on the excitation power and found this to be linear (Figure S15). While a linear power dependence is often considered to indicate a TADF process, we point out that this is evidently not the case here, as (i) the delayed fluorescence *reduces* upon heating up to 250 K instead of being thermally activated and (ii) its intensity evolution correlates with the aggregate concentration, while TADF should be independent of any aggregation effects. In fact, a linear power dependence is characteristic for TTA if the TTA process dominates over other radiative or nonradiative triplet decay channels.[62] For pulsed excitation with triplet lifetimes of 30 ms or longer, this condition is easily fullfilled. This is confirmed by the time dependence of the DF signal. The 200 K signals shows the plateau followed by the t^{-2} decay that is characteristic for the DF decay, which evolves as $([T_0]/(1 + [T_0]\gamma t))^2$, where $[T_0]$ is the initial triplet concentration and γ is the annihilation constant. At lower temperatures, transport becomes increasingly dispersive, thus reducing the slope toward t^{-1}.

Having established that TTA prevails from 5 K to close to 300 K, we now consider the temperature regime from 300 K onward (Figure 6c). It is evident that, upon heating, a thermally activated component emerges. Thus, it seems that there is a TADF component that becomes active above 300 K. The crossover between the regimes where TTA and where TADF prevail is around room temperature. For the analysis of the TADF kinetics it is important to establish whether any contribution dominates at 300 K. We have therefore measured the dependence of the decay transient on excitation power. A higher TTA rate due to a higher triplet concentration would alter the time where the plateau merges into the t^{-2} decay. We observe no change in the decay transients upon increasing the fluence from 0.3 to 30 μJ for a spot size of 4 mm diameter, even when using a more concentrated solution where aggregation should be stronger (see Figure S16). This suggests that at 300 K and above the decay kinetics in the "shorter" time range up to a few microseconds is controlled mostly by a monomolecular process such as TADF. At longer times above a few microseconds, where the decay merges into a t^{-2} dependence, TTA evidently still prevails. Figure 6d shows a fit to the PL decay considering a monoexponential decay with a fixed lifetime of 450 ns to account for TADF and a decay according to $[T_0/(1 + T_1 t)]^2$ to account for TTA. A fit to the prompt fluorescence yields a lifetime of about 9 ns. This and fits with other TADF lifetimes are available in the Supporting Information (Figure S16).

It is *not* possible to derive a rate for the reverse intersystem crossing, k_{RISC}, from the dynamics described above. Simply inserting the lifetime into the frequently used equations from the Monkman group, as is sometimes done, would give a nominal value of about 2×10^6 s^{-1}, which would be a high value for a ΔE_{ST} of 0.31 eV.[67,68] However, as has also been stressed by the Monkman group, in deriving these equations a number of approximations are made that only hold when the quantum yield for DF, Φ_{DF}, is about 4 times larger than that of the PF, Φ_{PF}. This

Table 1. Lifetime Data and Excited-State Energies for α-3BNOH in THF Solution and in Film

	in 7.6 × 10⁻⁵ M THF solution					at 1 wt % in PMMA				
	τ_p (ns)	$\tau_d{}^a$ (ns)	$E_{S1}{}^b$ (eV)	$E_{T1}{}^c$ (eV)	$\Delta E_{ST}{}^d$ (eV)	τ_p (ns)	$\tau_d{}^e$ (μs)	$E_{S1}{}^b$ (eV)	$E_{T1}{}^c$ (eV)	$\Delta E_{ST}{}^d$ (eV)
α-3BNOH	8.5	450	3.12	2.81	0.31	8.5	260	3.14	2.92	0.22

[a]λ_{exc} = 355 nm at 300 K under vacuum, prompt component τ_p and delayed component τ_d obtained using a single-exponential decays for each. [b]Obtained from the maxima of the PL steady-state spectrum at 77 K, λ_{exc} = 335 nm. [c]Obtained from the maxima of the PL spectrum at 77 K, λ_{exc} = 355 nm. [d]$\Delta E_{ST} = E(S_1) - E(T_1)$. [e]Obtained by using a single exponential.
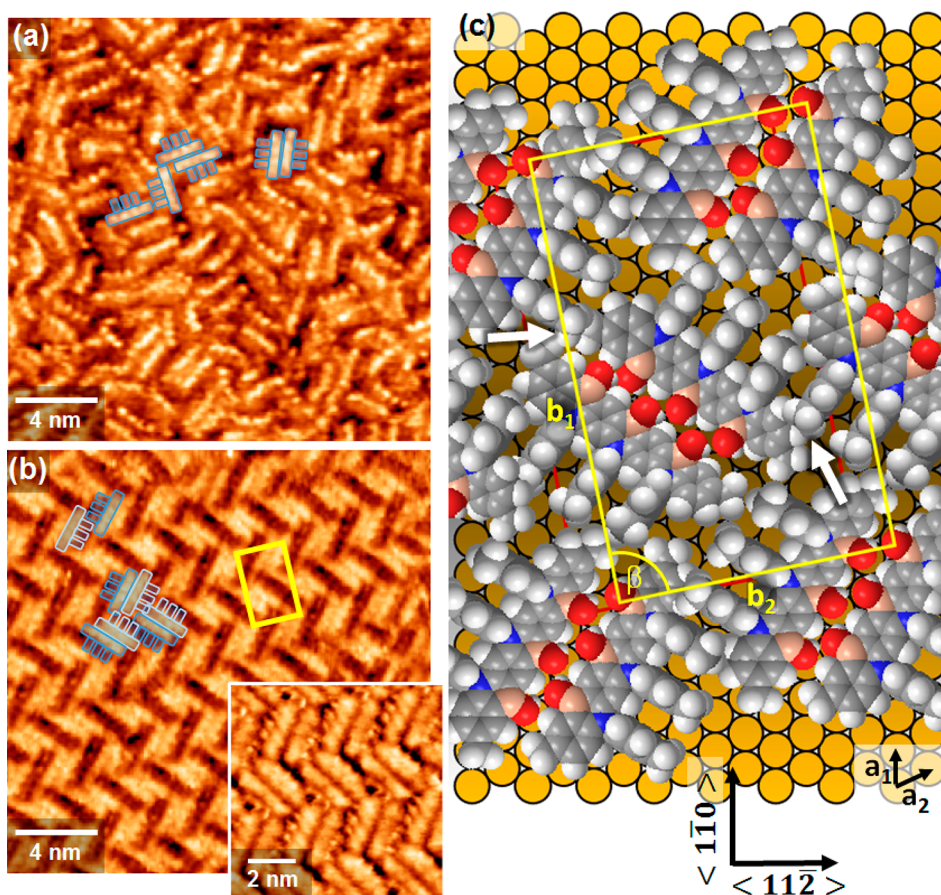

Figure 8. STM images of α-3BNOH monolayers on Au(111) prepared at 343 K from 400 μM DMF solution (a) and at room temperature from 150 μM DMF solution (b) with inset showing the layer at different tunneling contrast. The footprint of the molecules and their packing is indicated by the blue shapes. (c) Space-filling model of the ordered structure shown in (b). Arrows point to sterically crowded sites. Yellow rectangles in (b) and (c) indicate the unit cell. Tunneling parameters (U_{tip}/I): (a) +0.5 V/40 pA, (b) +0.268 V/30 pA (large image), +0.1 V/0.1 nA (inset).

is not the case for α-3BNOH. Rather, in Figure 6d, $\Phi_{DF} \approx 0.01\Phi_{PF}$, consistent with the ΔE_{ST} value and previous MR-TADF emitters.[48,69] We note that the TADF component seems to have an activation energy of only about 70 meV while the singlet−triplet splitting is in the range of 300 meV. This discrepancy has previously been accounted for by mixing with higher-lying excited states.[68] SCS-CC2 calculations predict the presence of two higher-lying triplet states of energies intermediate between T₁ and S₁, each of which has MR-TADF character (Figure S12). Here, the low value may also relate to the fact that the TADF component superimposes on the TTA component. The reduction of the TTA contribution with increasing temperature due to the dissolution of any aggregates also reduces the observed increase in TADF, and the two processes are difficult to disentangle.

For electroluminescent device applications, it is essential to know how these properties translate into films. Figure 7 shows

the spectra and transients obtained for α-3BNOH dispersed (doped) at 1 wt % into poly(methyl methacrylate) (PMMA).

Comparison with the solution spectra shown in Figures 4 and 5 shows that the long-lived component peaking at about 425 nm (2.92 eV) at 77 K is the phosphorescence signal, and the short-lived band peaking around 395 nm (3.14 eV) is the fluorescence. In the PMMA matrix, the ratio between the integrated delayed fluorescence signal and the integrated prompt fluorescence increases significantly, so that $\Phi_{DF} \approx 0.20\Phi_{PF}$. The FWHM is 0.25 eV (32 nm), i.e., nearly unaltered compared to the value in solution. The singlet−triplet gap, ΔE_{ST}, in the 1 wt % emitter doped in PMMA film is 0.22 eV, which is about 100 meV smaller compared to that in THF solution. Such shifts are common for charge-transfer type states and result from different polarities of the solvent and matrix. The short-lived feature at 525 nm observed at 77 K is some emission from remnant excimers or aggregates that disappears below a microseconds time scale (see Figure S17). It is gratifying that this does not prevail at room

temperature, thus preserving the deep blue emission color with CIE coordinates of $x = 0.17$ and $y = 0.01$ when dispersed at 1 wt % in PMMA. This represents a blue-shift compared to DABNA-1,[48] which has CIE coordinates of (0.13, 0.09) in the electroluminescent device, at the expense of a slightly larger FWHM (0.25 eV or 32 nm for α-3BNOH compared to 0.20 eV or 28 nm for DABNA-1 in the OLED).

The PL transients of the doped film show three distinct regimes. First, we observe a prompt decay component with a lifetime of 8.5 ns, identical to that in solution. Second, from about 100 ns to several microseconds we observe a decay of unclear origin. Finally, toward longer times there is an exponential decay that is temperature activated. At room temperature, the lifetime of this monoexponential decay is about 260 μs (see Figure S18a). Evaluating the thermal activation of the long-lived decay gives an activation energy of 220 meV, which matches with the observed ΔE_{ST} (see Figure S18c). It does not show any dependence on incident light intensity (see Figure S18b), identifying it as a monomolecular process. This, in combination with the thermal activation with an energy that matches the singlet−triplet splitting, strongly suggests the 260 μs lifetime to be a TADF signal. If fitted with a single-exponential decay, then the signal in the intermediate range from about 100 ns to several microseconds has a lifetime on the order of 0.5 μs, though an interpretation as a dispersive decay following a t^{-1} law would also be possible. It shows a small dependence on intensity (see Figure S18b). Evidently, more detailed follow-up studies beyond the scope of this investigation are required to unambiguously assign this intermediate feature. The photophysical data in solution and film are summarized in Table 1. Solvatochromic measurements have also been performed in solution (Figure S19), yet they show no systematic shift with solvent polarity, in agreement with the short-range charge transfer observed in the S_1 excited state (see Figure 3).

We next performed scanning tunneling microscopy (STM) measurements to study the self-assembly process of α-3BNOH on a Au(111) surface. The focus was on the first layer which, through templating and modification of chemical interactions, is critical for the growth of thin films.[70−72] Samples prepared at two different temperatures (RT and 343 K) and a range of concentrations were investigated. The STM images at submolecular resolution of layers prepared from solutions of α-3BNOH (Figure 8) reveal a pronounced influence of concentration on the order of the layers as illustrated in Figure 8 whereas no noticeable influence of the preparation temperature was observed. Higher concentrations yield disordered layers as evidenced by Figure 8a. In contrast, a highly crystalline herringbone structure is formed at the lower concentration (Figure 8b), and in the intermediate concentration range above 200 μM the two morphologies can coexist. In the STM images of both the disordered and crystalline layers of the individual molecules are clearly discernible with some of them overlaid by a footprint of the molecules outlining the acene backbone and the three tolyl units. It is noted that the submolecular resolution is dependent on tip conditions as well as tunneling parameters. In the disordered layer the four benzene rings of the heptacene backbone are clearly resolved. A somewhat different tunneling contrast is seen in the large image of the crystalline layer where, even though less pronounced, the backbone is still resolved but also individual tolyl moieties show up as protrusions. The latter become even more clear using another set of tunneling parameters (inset of Figure 8b).

The basic units of the ordered layer consist of dimers with two achiral α-3BNOH molecules arranged in a staggered fashion to yield two chiral enantiomeric entities. As seen from the molecular model displayed in Figure 8c, such a dimerization is favored by the contour of the molecules and their supra-molecular interactions comprising OH···H and C−H···O bonding. The herringbone structure is the result of an alternating arrangement of the enantiomeric dimers. While a herringbone packing has been observed for other acene monolayers like rubrene[73] or pentacene,[74] the present case is different as instead of an achiral monomer chiral dimers are the units underlying the structure. The formation of dimers is impeded at the higher concentration due to kinetic barriers arising from interlocking of the molecules before they can arrange into an ordered structure. This evidences that pairing of the molecules is a process occurring at the surface and not in the bulk solution.

Looking at the structural model of Figure 8c, the major intermolecular interactions in the monolayers are those resulting in dimer formation. Interactions between different dimers seem to be comparably weak, even though not negligible as the alignment of the tolyl groups of adjacent molecules suggest as illustrated in the top left corner of Figure 8b. Also, sterical hindrance is likely to play a role (sites marked by arrows in Figure 8c), which would require some conformational adjustment. Therefore, the interaction between the acene backbone and the metal surface is considered the major driving force to minimize the energy of the system by maximizing coverage. Other dimer arrangements such as a linear structure mediated by interactions of tolyl moieties would result in a more open structure and, therefore, a lower coverage. The registry between substrate and lattice of the α-3BNOH layer also plays a role as domains are aligned along well-defined directions of the substrate. On the basis of the STM data, the unit cell marked by the yellow rectangles is proposed. Containing four molecules (211 Å^2 per molecule), it is an essentially rectangular unit cell with parameters of $b_1 = \sqrt{163}\, a = 36.9$ Å, $b_2 = 3\sqrt{7}\, a = 22.9$ Å (a as the unit cell parameter of the Au(111) surface, 2.89 Å), and $\beta = 90.8°$, in matrix notation (14 −3, −3 9). This means the presence of mirror domains with b_2 off the $\langle 11\bar{2}\rangle$ direction by $\pm10.9°$. While it is well-known that achiral molecules can assemble on surfaces to form chiral domains,[75] α-3BNOH is different as mirror domains are enantiomorphic structures of racemix mixtures of the chiral dimers, analogous to the case of heptahelicenes where this has been observed for a mixture of enantiomeric monomers.[76] As far as the assembly process is concerned, it is not clear at present whether the dimers preform and attach to or individual molecules lock into a growing domain. Detailed concentration-dependent studies will provide further insight into the mechanism of film formation.

■ CONCLUSIONS

In summary, a linearly extended B,N-doped heptacene (α-3BNOH) has been synthesized via electrophilic arene borylation. Starting from p-toluidine, we obtained α-3BNOH in three steps in good yields through easy-to-access chemical reactions. High thermal stabilty ($T_d = 554$ °C) was exhibited by this compound. The multiresonant TADF property of α-3BNOH has been investigated by combining results from state-of-the art quantum-chemical calculations and temperature-dependent emission decay measurements. Our heptacene

derivative presents a near-UV emission profile in solutions with a narrow emission band. Compared to the reported MR-TADF emitter ν-DABNA, which is by far the highest performing MR-TADF compound in terms of a fast fluorescence rate ($k_F = 2.0 \times 10^8$ s^{-1}) short delayed lifetime ($\tau_d = 4.1$ μs) and efficient rISC ($k_{RISC} = 2.0 \times 10^5$ s^{-1}),[46] α-3BNOH possesses an order of magnitude shorter delayed lifetime of only 450 ± 10 ns in solution. In thin films, the deep blue color with CIE coordinates of (0.17, 0.01) is gratifyingly preserved. α-3BNOH thus essentially possesses the optoelectronic requirement for a deep blue TADF material in terms of high band gap. In addition, α-3BNOH presented an attractive combination of TADF and TTA in a single material, which can lead to a hybrid, long-lived, and highly efficient deep blue material for OLEDs. With the help of theoretical calculations we demonstrated the dependence of ΔE_{ST} and optical energy gap in linear, heteroatom-doped acenes through controlling the position of donor and acceptor atoms in the acene core. Finally, the quality of α-3BNOH layers on a Au(111) surface is critically dependent on the preparation conditions. Remarkably, a highly crystalline layer exhibiting a hierarchical organization of the achiral molecule to enantiomeric dimers and ordering to a racemic chiral structure is observed.

■ ASSOCIATED CONTENT

Ⓢ Supporting Information

The Supporting Information is available free of charge at https://pubs.acs.org/doi/10.1021/jacs.9b13704.

> ^{1}H NMR, ^{13}C NMR, and HRMS spectra of all new compounds; supplementary computational data and coordinates; supplementary photophysical data (PDF)
>
> Crystallographic data for α-3BNOH (CIF)

■ AUTHOR INFORMATION

Corresponding Authors

Eli Zysman-Colman − *Organic Semiconductor Centre, EaStCHEM School of Chemistry, University of St. Andrews, St. Andrews, U.K. KY16 9ST;* ⓞ orcid.org/0000-0001-7183-6022; Email: eli.zysman-colman@st-andrews.ac.uk

Anna Köhler − *Soft Matter Optoelectronics, University of Bayreuth, 95447 Bayreuth, Germany;* ⓞ orcid.org/0000-0001-5029-4420; Email: anna.koehler@uni-bayreuth.de

Manfred Buck − *Organic Semiconductor Centre, EaStCHEM School of Chemistry, University of St. Andrews, St. Andrews, U.K. KY16 9ST;* Email: mb45@st-andrews.ac.uk

Yoann Olivier − *Laboratory for Chemistry of Novel Materials, University of Mons, 7000 Mons, Belgium; Unité de Chimie Physique Théorique et Structurale & Laboratoire de Physique du Solide, Namur Institute of Structured Matter, Université de Namur, 5000 Namur, Belgium;* Email: yoann.olivier@unamur.be

Authors

Subeesh Madayanad Suresh − *Organic Semiconductor Centre, EaStCHEM School of Chemistry, University of St. Andrews, St. Andrews, U.K. KY16 9ST*

Eimantas Duda − *Soft Matter Optoelectronics, University of Bayreuth, 95447 Bayreuth, Germany*

David Hall − *Organic Semiconductor Centre, EaStCHEM School of Chemistry, University of St. Andrews, St. Andrews, U.K. KY16 9ST; Laboratory for Chemistry of Novel Materials, University of Mons, 7000 Mons, Belgium*

Zhen Yao − *Organic Semiconductor Centre, EaStCHEM School of Chemistry, University of St. Andrews, St. Andrews, U.K. KY16 9ST*

Sergey Bagnich − *Soft Matter Optoelectronics, University of Bayreuth, 95447 Bayreuth, Germany*

Alexandra M. Z. Slawin − *Organic Semiconductor Centre, EaStCHEM School of Chemistry, University of St. Andrews, St. Andrews, U.K. KY16 9ST*

Heinz Bässler − *BIMF, University of Bayreuth, 95447 Bayreuth, Germany*

David Beljonne − *Laboratory for Chemistry of Novel Materials, University of Mons, 7000 Mons, Belgium;* ⓞ orcid.org/0000-0002-2989-3557

Complete contact information is available at:
https://pubs.acs.org/10.1021/jacs.9b13704

Notes

The authors declare no competing financial interest.
The research data supporting this publication can be accessed at https://doi.org/10.17630/61d22464-e20e-4914-a7ff-31e2858034a6

■ REFERENCES

(1) Geim, A. K.; Novoselov, K. S. The rise of graphene. *Nat. Mater.* **2007**, *6* (3), 183−191.

(2) Geim, A. K. Graphene: Status and Prospects. *Science* **2009**, *324* (5934), 1530−1534.

(3) Lemine, A. S.; Zagho, M. M.; Altahtamouni, T. M.; Bensalah, N. Graphene a promising electrode material for supercapacitors—A review. *Int. J. Energy Res.* **2018**, *42* (14), 4284−4300.

(4) Wang, X.-Y.; Narita, A.; Müllen, K. Precision synthesis versus bulk-scale fabrication of graphenes. *Nat. Rev. Chem.* **2018**, *2*, 0100.

(5) Xu, B.; Yue, S.; Sui, Z.; Zhang, X.; Hou, S.; Cao, G.; Yang, Y. What is the choice for supercapacitors: graphene or graphene oxide? *Energy Environ. Sci.* **2011**, *4* (8), 2826−2830.

(6) Fan, W.; Xia, Y.-Y.; Tjiu, W. W.; Pallathadka, P. K.; He, C.; Liu, T. Nitrogen-doped graphene hollow nanospheres as novel electrode materials for supercapacitor applications. *J. Power Sources* **2013**, *243*, 973−981.

(7) Karthika, P.; Rajalakshmi, N.; Dhathathreyan, K. S. Phosphorus-Doped Exfoliated Graphene for Supercapacitor Electrodes. *J. Nanosci. Nanotechnol.* **2013**, *13* (3), 1746−1751.

(8) Yang, S.; Song, X.; Zhang, P.; Gao, L. Facile Synthesis of Nitrogen-Doped Graphene-Ultrathin MnO2 Sheet Composites and Their Electrochemical Performances. *ACS Appl. Mater. Interfaces* **2013**, *5* (8), 3317−3322.

(9) Wu, Z.-S.; Ren, W.; Xu, L.; Li, F.; Cheng, H.-M. Doped Graphene Sheets As Anode Materials with Superhigh Rate and Large Capacity for Lithium Ion Batteries. *ACS Nano* **2011**, *5* (7), 5463−5471.

(10) Zhang, C.; Mahmood, N.; Yin, H.; Liu, F.; Hou, Y. Synthesis of Phosphorus-Doped Graphene and its Multifunctional Applications for Oxygen Reduction Reaction and Lithium Ion Batteries. *Adv. Mater.* **2013**, *25* (35), 4932−4937.

(11) Wang, Z.-L.; Xu, D.; Wang, H.-G.; Wu, Z.; Zhang, X.-B. In Situ Fabrication of Porous Graphene Electrodes for High-Performance Energy Storage. *ACS Nano* **2013**, *7* (3), 2422−2430.

(12) Nethravathi, C.; Rajamathi, C. R.; Rajamathi, M.; Gautam, U. K.; Wang, X.; Golberg, D.; Bando, Y. N-Doped Graphene-VO2(B) Nanosheet-Built 3D Flower Hybrid for Lithium Ion Battery. *ACS Appl. Mater. Interfaces* **2013**, *5* (7), 2708−2714.

(13) Qu, L.; Liu, Y.; Baek, J.-B.; Dai, L. Nitrogen-Doped Graphene as Efficient Metal-Free Electrocatalyst for Oxygen Reduction in Fuel Cells. *ACS Nano* **2010**, *4* (3), 1321−1326.

(14) Gao, H.; Liu, Z.; Song, L.; Guo, W.; Gao, W.; Ci, L.; Rao, A.; Quan, W.; Vajtai, R.; Ajayan, P. M. Synthesis of S-doped graphene by liquid precursor. *Nanotechnology* **2012**, *23* (27), 275605.

(15) Xu, J.; Dong, G.; Jin, C.; Huang, M.; Guan, L. Sulfur and nitrogen co-doped, few-layered graphene oxide as a highly efficient electrocatalyst for the oxygen-reduction reaction. *ChemSusChem* **2013**, *6* (3), 493−499.

(16) Jeon, I.-Y.; Choi, H.-J.; Choi, M.; Seo, J.-M.; Jung, S.-M.; Kim, M.-J.; Zhang, S.; Zhang, L.; Xia, Z.; Dai, L.; Park, N.; Baek, J.-B. Facile, scalable synthesis of edge-halogenated graphene nanoplatelets as efficient metal-free eletrocatalysts for oxygen reduction reaction. *Sci. Rep.* **2013**, *3*, 1810.

(17) Li, X.; Fan, L.; Li, Z.; Wang, K.; Zhong, M.; Wei, J.; Wu, D.; Zhu, H. Boron Doping of Graphene for Graphene-Silicon p-n Junction Solar Cells. *Adv. Energy Mater.* **2012**, *2* (4), 425−429.

(18) Xue, Y.; Liu, J.; Chen, H.; Wang, R.; Li, D.; Qu, J.; Dai, L. Nitrogen-Doped Graphene Foams as Metal-Free Counter Electrodes in High-Performance Dye-Sensitized Solar Cells. *Angew. Chem., Int. Ed.* **2012**, *51* (48), 12124−12127.

(19) Das, S.; Sudhagar, P.; Verma, V.; Song, D.; Ito, E.; Lee, S. Y.; Kang, Y. S.; Choi, W. Amplifying Charge-Transfer Characteristics of Graphene for Triiodide Reduction in Dye-Sensitized Solar Cells. *Adv. Funct. Mater.* **2011**, *21* (19), 3729−3736.

(20) Kwon, O. S.; Park, S. J.; Hong, J.-Y.; Han, A. R.; Lee, J. S.; Lee, J. S.; Oh, J. H.; Jang, J. Flexible FET-Type VEGF Aptasensor Based on Nitrogen-Doped Graphene Converted from Conducting Polymer. *ACS Nano* **2012**, *6* (2), 1486−1493.

(21) Wang, Y.; Shao, Y.; Matson, D. W.; Li, J.; Lin, Y. Nitrogen-Doped Graphene and Its Application in Electrochemical Biosensing. *ACS Nano* **2010**, *4* (4), 1790−1798.

(22) Sheng, Z.-H.; Zheng, X.-Q.; Xu, J.-Y.; Bao, W.-J.; Wang, F.-B.; Xia, X.-H. Electrochemical sensor based on nitrogen doped graphene: Simultaneous determination of ascorbic acid, dopamine and uric acid. *Biosens. Bioelectron.* **2012**, *34* (1), 125−131.

(23) Zhang, Y.-H.; Chen, Y.-B.; Zhou, K.-G.; Liu, C.-H.; Zeng, J.; Zhang, H.-L.; Peng, Y. Improving gas sensing properties of graphene by introducing dopants and defects: a first-principles study. *Nanotechnology* **2009**, *20* (18), 185504.

(24) Cai, J.; Ruffieux, P.; Jaafar, R.; Bieri, M.; Braun, T.; Blankenburg, S.; Muoth, M.; Seitsonen, A. P.; Saleh, M.; Feng, X.; Müllen, K.; Fasel, R. Atomically precise bottom-up fabrication of graphene nanoribbons. *Nature* **2010**, *466* (7305), 470−473.

(25) Cloke, R. R.; Marangoni, T.; Nguyen, G. D.; Joshi, T.; Rizzo, D. J.; Bronner, C.; Cao, T.; Louie, S. G.; Crommie, M. F.; Fischer, F. R.

(26) Kawai, S.; Saito, S.; Osumi, S.; Yamaguchi, S.; Foster, A. S.; Spijker, P.; Meyer, E. Atomically controlled substitutional boron-doping of graphene nanoribbons. *Nat. Commun.* **2015**, *6* (1), 8098.

(27) Sánchez-Sánchez, C.; Brüller, S.; Sachdev, H.; Müllen, K.; Krieg, M.; Bettinger, H. F.; Nicolaï, A.; Meunier, V.; Talirz, L.; Fasel, R.; Ruffieux, P. On-Surface Synthesis of BN-Substituted Heteroaromatic Networks. *ACS Nano* **2015**, *9* (9), 9228−9235.

(28) Smalley, R. E.; Li, Y.; Moore, V. C.; Price, B. K.; Colorado, R.; Schmidt, H. K.; Hauge, R. H.; Barron, A. R.; Tour, J. M. Single Wall Carbon Nanotube Amplification: En Route to a Type-Specific Growth Mechanism. *J. Am. Chem. Soc.* **2006**, *128* (49), 15824−15829.

(29) Fort, E. H.; Scott, L. T. One-Step Conversion of Aromatic Hydrocarbon Bay Regions into Unsubstituted Benzene Rings: A Reagent for the Low-Temperature, Metal-Free Growth of Single-Chirality Carbon Nanotubes. *Angew. Chem., Int. Ed.* **2010**, *49* (37), 6626−6628.

(30) Yu, X.; Zhang, J.; Choi, W.; Choi, J.-Y.; Kim, J. M.; Gan, L.; Liu, Z. Cap Formation Engineering: From Opened C60 to Single-Walled Carbon Nanotubes. *Nano Lett.* **2010**, *10* (9), 3343−3349.

(31) Numano, M.; Nagami, N.; Nakatsuka, S.; Katayama, T.; Nakajima, K.; Tatsumi, S.; Yasuda, N.; Hatakeyama, T. Synthesis of Boronate-Based Benzo[fg]tetracene and Benzo[hi]hexacene via Demethylative Direct Borylation. *Chem. - Eur. J.* **2016**, *22* (33), 11574−11577.

(32) Wang, X.-Y.; Narita, A.; Zhang, W.; Feng, X.; Müllen, K. Synthesis of Stable Nanographenes with OBO-Doped Zigzag Edges Based on Tandem Demethylation-Electrophilic Borylation. *J. Am. Chem. Soc.* **2016**, *138* (29), 9021−9024.

(33) Hatakeyama, T.; Hashimoto, S.; Seki, S.; Nakamura, M. Synthesis of BN-Fused Polycyclic Aromatics via Tandem Intramolecular Electrophilic Arene Borylation. *J. Am. Chem. Soc.* **2011**, *133* (46), 18614−18617.

(34) Hatakeyama, T.; Hashimoto, S.; Oba, T.; Nakamura, M. Azaboradibenzo[6]helicene: Carrier Inversion Induced by Helical Homochirality. *J. Am. Chem. Soc.* **2012**, *134* (48), 19600−19603.

(35) Wang, X.; Zhang, F.; Liu, J.; Tang, R.; Fu, Y.; Wu, D.; Xu, Q.; Zhuang, X.; He, G.; Feng, X. Ladder-Type BN-Embedded Hetero-acenes with Blue Emission. *Org. Lett.* **2013**, *15* (22), 5714−5717.

(36) Wang, X.-Y.; Zhuang, F.-D.; Wang, X.-C.; Cao, X.-Y.; Wang, J.-Y.; Pei, J. Synthesis, structure and properties of C3-symmetric hetero-superbenzene with three BN units. *Chem. Commun.* **2015**, *51* (21), 4368−4371.

(37) Li, G.; Xiong, W.-W.; Gu, P.-Y.; Cao, J.; Zhu, J.; Ganguly, R.; Li, Y.; Grimsdale, A. C.; Zhang, Q. 1,5,9-Triaza-2,6,10-triphenylboracor-onene: BN-Embedded Analogue of Coronene. *Org. Lett.* **2015**, *17* (3), 560−563.

(38) Crossley, D. L.; Cade, I. A.; Clark, E. R.; Escande, A.; Humphries, M. J.; King, S. M.; Vitorica-Yrezabal, I.; Ingleson, M. J.; Turner, M. L. Enhancing electron affinity and tuning band gap in donor-acceptor organic semiconductors by benzothiadiazole directed C-H borylation. *Chem. Sci.* **2015**, *6* (9), 5144−5151.

(39) Crossley, D. L.; Vitorica-Yrezabal, I.; Humphries, M. J.; Turner, M. L.; Ingleson, M. J. Highly Emissive Far Red/Near-IR Fluorophores Based on Borylated Fluorene-Benzothiadiazole Donor-Acceptor Materials. *Chem. - Eur. J.* **2016**, *22* (35), 12439−12448.

(40) Furukawa, S.; Kobayashi, J.; Kawashima, T. Development of a Sila-Friedel-Crafts Reaction and Its Application to the Synthesis of Dibenzosilole Derivatives. *J. Am. Chem. Soc.* **2009**, *131* (40), 14192−14193.

(41) Hashimoto, S.; Nakatsuka, S.; Nakamura, M.; Hatakeyama, T. Construction of a Highly Distorted Benzene Ring in a Double Helicene. *Angew. Chem., Int. Ed.* **2014**, *53* (51), 14074−14076.

(42) Miyamoto, F.; Nakatsuka, S.; Yamada, K.; Nakayama, K.-i.; Hatakeyama, T. Synthesis of Boron-Doped Polycyclic Aromatic Hydrocarbons by Tandem Intramolecular Electrophilic Arene Borylation. *Org. Lett.* **2015**, *17* (24), 6158−6161.

Site-Specific Substitutional Boron Doping of Semiconducting Armchair Graphene Nanoribbons. *J. Am. Chem. Soc.* **2015**, *137* (28), 8872−8875.

(43) Fujimoto, K.; Oh, J.; Yorimitsu, H.; Kim, D.; Osuka, A. Directly Diphenylborane-Fused Porphyrins. *Angew. Chem., Int. Ed.* **2016**, *55* (9), 3196−3199.

(44) Wang, X.; Zhang, F.; Schellhammer, K. S.; Machata, P.; Ortmann, F.; Cuniberti, G.; Fu, Y.; Hunger, J.; Tang, R.; Popov, A. A.; Berger, R.; Müllen, K.; Feng, X. Synthesis of NBN-Type Zigzag-Edged Polycyclic Aromatic Hydrocarbons: 1,9-Diaza-9a-boraphenalene as a Structural Motif. *J. Am. Chem. Soc.* **2016**, *138* (36), 11606−11615.

(45) Hirai, H.; Nakajima, K.; Nakatsuka, S.; Shiren, K.; Ni, J.; Nomura, S.; Ikuta, T.; Hatakeyama, T. One-Step Borylation of 1,3-Diaryloxybenzenes Towards Efficient Materials for Organic Light-Emitting Diodes. *Angew. Chem., Int. Ed.* **2015**, *54* (46), 13581−13585.

(46) Kondo, Y.; Yoshiura, K.; Kitera, S.; Nishi, H.; Oda, S.; Gotoh, H.; Sasada, Y.; Yanai, M.; Hatakeyama, T. Narrowband deep-blue organic light-emitting diode featuring an organoboron-based emitter. *Nat. Photonics* **2019**, *13* (10), 678−682.

(47) Nakatsuka, S.; Gotoh, H.; Kinoshita, K.; Yasuda, N.; Hatakeyama, T. Divergent Synthesis of Heteroatom-Centered 4,8,12-Triazatriangulenes. *Angew. Chem., Int. Ed.* **2017**, *56* (18), 5087−5090.

(48) Hatakeyama, T.; Shiren, K.; Nakajima, K.; Nomura, S.; Nakatsuka, S.; Kinoshita, K.; Ni, J.; Ono, Y.; Ikuta, T. Ultrapure Blue Thermally Activated Delayed Fluorescence Molecules: Efficient HOMO-LUMO Separation by the Multiple Resonance Effect. *Adv. Mater.* **2016**, *28* (14), 2777−2781.

(49) Matsui, K.; Oda, S.; Yoshiura, K.; Nakajima, K.; Yasuda, N.; Hatakeyama, T. One-Shot Multiple Borylation toward BN-Doped Nanographenes. *J. Am. Chem. Soc.* **2018**, *140* (4), 1195−1198.

(50) Han, S. H.; Jeong, J. H.; Yoo, J. W.; Lee, J. Y. Ideal blue thermally activated delayed fluorescence emission assisted by a thermally activated delayed fluorescence assistant dopant through a fast reverse intersystem crossing mediated cascade energy transfer process. *J. Mater. Chem. C* **2019**, *7* (10), 3082−3089.

(51) Pershin, A.; Hall, D.; Lemaur, V.; Sancho-Garcia, J.-C.; Muccioli, L.; Zysman-Colman, E.; Beljonne, D.; Olivier, Y. Highly emissive excitons with reduced exchange energy in thermally activated delayed fluorescent molecules. *Nat. Commun.* **2019**, *10* (1), 597.

(52) Hirai, M.; Tanaka, N.; Sakai, M.; Yamaguchi, S. Structurally Constrained Boron-, Nitrogen-, Silicon-, and Phosphorus-Centered Polycyclic π-Conjugated Systems. *Chem. Rev.* **2019**, *119* (14), 8291−8331.

(53) Agou, T.; Kobayashi, J.; Kawashima, T. Syntheses, Structure, and Optical Properties of Ladder-Type Fused Azaborines. *Org. Lett.* **2006**, *8* (11), 2241−2244.

(54) Sambiagio, C.; Marsden, S. P.; Blacker, A. J.; McGowan, P. C. Copper catalysed Ullmann type chemistry: from mechanistic aspects to modern development. *Chem. Soc. Rev.* **2014**, *43* (10), 3525−3550.

(55) Ruiz-Castillo, P.; Buchwald, S. L. Applications of Palladium-Catalyzed C-N Cross-Coupling Reactions. *Chem. Rev.* **2016**, *116* (19), 12564−12649.

(56) Connelly, N. G.; Geiger, W. E. Chemical Redox Agents for Organometallic Chemistry. *Chem. Rev.* **1996**, *96* (2), 877−910.

(57) Cardona, C. M.; Li, W.; Kaifer, A. E.; Stockdale, D.; Bazan, G. C. Electrochemical Considerations for Determining Absolute Frontier Orbital Energy Levels of Conjugated Polymers for Solar Cell Applications. *Adv. Mater.* **2011**, *23* (20), 2367−2371.

(58) Gierschner, J.; Cornil, J.; Egelhaaf, H.-J. Optical Bandgaps of π-Conjugated Organic Materials at the Polymer Limit: Experiment and Theory. *Adv. Mater.* **2007**, *19* (2), 173−191.

(59) Gierschner, J.; Mack, H.-G.; Lüer, L.; Oelkrug, D. Fluorescence and absorption spectra of oligophenylenevinylenes: Vibronic coupling, band shapes, and solvatochromism. *J. Chem. Phys.* **2002**, *116* (19), 8596−8609.

(60) Marcus, M.; Milward, J. D.; Köhler, A.; Barford, W. Structural Information for Conjugated Polymers from Optical Modeling. *J. Phys. Chem. A* **2018**, *122* (14), 3621−3625.

(61) Raithel, D.; Simine, L.; Pickel, S.; Schötz, K.; Panzer, F.; Baderschneider, S.; Schiefer, D.; Lohwasser, R.; Köhler, J.; Thelakkat, M.; Sommer, M.; Köhler, A.; Rossky, P. J.; Hildner, R. Direct observation of backbone planarization via side-chain alignment in single

bulky-substituted polythiophenes. *Proc. Natl. Acad. Sci. U. S. A.* **2018**, *115* (11), 2699.

(62) Köhler, A.; Bässler, H. The Electronic Structure of Organic Semiconductors. In *Electronic Processes in Organic Semiconductors*; Wiley-VCH: 2015.

(63) Mondal, R.; Tönshoff, C.; Khon, D.; Neckers, D. C.; Bettinger, H. F. Synthesis, Stability, and Photochemistry of Pentacene, Hexacene, and Heptacene: A Matrix Isolation Study. *J. Am. Chem. Soc.* **2009**, *131* (40), 14281−14289.

(64) Payne, M. M.; Parkin, S. R.; Anthony, J. E. Functionalized Higher Acenes: Hexacene and Heptacene. *J. Am. Chem. Soc.* **2005**, *127* (22), 8028−8029.

(65) Xiao, Y.; Mague, J. T.; Schmehl, R. H.; Haque, F. M.; Pascal, R. A., Jr. Dodecaphenyltetracene. *Angew. Chem., Int. Ed.* **2019**, *58* (9), 2831−2833.

(66) Müller, M.; Rüdiger, E. C.; Koser, S.; Tverskoy, O.; Rominger, F.; Hinkel, F.; Freudenberg, J.; Bunz, U. H. F. Butterfly Wings" Stabilize Heptacene. *Chem. - Eur. J.* **2018**, *24* (32), 8087−8091.

(67) Haase, N.; Danos, A.; Pflumm, C.; Morherr, A.; Stachelek, P.; Mekic, A.; Brütting, W.; Monkman, A. P. Kinetic Modeling of Transient Photoluminescence from Thermally Activated Delayed Fluorescence. *J. Phys. Chem. C* **2018**, *122* (51), 29173−29179.

(68) Dias, F. B.; Santos, J.; Graves, D. R.; Data, P.; Nobuyasu, R. S.; Fox, M. A.; Batsanov, A. S.; Palmeira, T.; Berberan-Santos, M. N.; Bryce, M. R.; Monkman, A. P. The Role of Local Triplet Excited States and D-A Relative Orientation in Thermally Activated Delayed Fluorescence: Photophysics and Devices. *Advanced Science* **2016**, *3* (12), 1600080.

(69) Hall, D.; Suresh, S. M.; dos Santos, P. L.; Duda, E.; Bagnich, S.; Pershin, A.; Rajamalli, P.; Cordes, D. B.; Slawin, A. M. Z.; Beljonne, D.; Köhler, A.; Samuel, I. D. W.; Olivier, Y.; Zysman-Colman, E. Improving Processability and Efficiency of Resonant TADF Emitters: A Design Strategy. *Adv. Opt. Mater.* **2020**, *8* (2), 1901627.

(70) Kanjilal, A.; Ottaviano, L.; Di Castro, V.; Beccari, M.; Betti, M. G.; Mariani, C. Pentacene Grown on Self-Assembled Monolayer: Adsorption Energy, Interface Dipole, and Electronic Properties. *J. Phys. Chem. C* **2007**, *111* (1), 286−293.

(71) Mänz, A.; Hauke, A. A.; Witte, G. Copper Phthalocyanine as Contact Layers for Pentacene Films Grown on Coinage Metals. *J. Phys. Chem. C* **2018**, *122* (4), 2165−2172.

(72) Skomski, D.; Tait, S. L. Interfacial Organic Layers for Chemical Stability and Crystalline Ordering of Thiophene and Carboxyl Films on a Metal Surface. *J. Phys. Chem. C* **2014**, *118* (3), 1594−1601.

(73) Luo, S. R.; Yau, S. L.; Kumaresan, P.; Vegiraju, S.; Chen, M.-C. Scanning Tunneling Microscopy Examination of Rubrene Deposited on Au(111) in Aqueous Solution. *J. Phys. Chem. C* **2015**, *119* (3), 1376−1381.

(74) Smerdon, J.; Bode, M.; Guisinger, N.; Guest, J. Monolayer and bilayer pentacene on Cu(111). *Phys. Rev. B: Condens. Matter Mater. Phys.* **2011**, *84*, 165436.

(75) Barlow, S. M.; Raval, R. Complex organic molecules at metal surfaces: bonding, organisation and chirality. *Surf. Sci. Rep.* **2003**, *50* (6), 201−341.

(76) Fasel, R.; Parschau, M.; Ernst, K.-H. Amplification of chirality in two-dimensional enantiomorphous lattices. *Nature* **2006**, *439* (7075), 449−452.